Geophysical Journal International

Geophys. J. Int. (2022) **229,** 589–604
Advance Access publication 2021 November 10
GJI Marine Geosciences and Applied Geophysics

https://doi.org/10.1093/gji/ggab462

Subaqueous fault scarps of the North Anatolian Fault in the Gulf of Saros (NE Aegean); where is the western limit of the 1912 Mürefte-Şarköy earthquake rupture?

M. Ersen Aksoy [1], Mustapha Meghraoui,[2,3] Alina Polonia,[4] M. Namık Çağatay,[5] Aslı Zeynep Yavuzoğlu,[6] Şebnem Önder,[7] Umut B. Ülgen[5,8] and Luca Gasperini[4]

[1] *Department of Geological Engineering, Muğla Sıtkı Koçman University,* 48000 *Muğla, Turkey. E-mail: ersenaksoy@mu.edu.tr*
[2] *Université de Strasbourg, CNRS, ITES, UMR* 7063, 67084 *Strasbourg, France*
[3] *Université de Strasbourg, CNRS, EOST, UAR* 830, 67084 *Strasbourg, France*
[4] *Istituto Di Scienze Marine, Consiglio Nazionale Delle, Ricerche (ISMAR-CNR),* 40129 *Bologna, Italy*
[5] *EMCOL Applied Research Centre, İstanbul Technical University,* 34467 *Istanbul, Turkey*
[6] *Marine Department, General Directorate of Mineral Research and Exploration of Turkey,* 06530 *Ankara, Turkey*
[7] *Çanakkale Onsekiz Mart University, Geophysical Engineering Department,* 17100 *Çanakkale, Turkey*
[8] *Medithermal Energy,* 34860 *Istanbul, Turkey*

Accepted 2021 October 30. Received 2021 October 17; in original form 2021 May 24

SUMMARY

The westernmost segment of the North Anatolian fault in NW Turkey lies mostly offshore, in the Sea of Marmara and the Gulf of Saros (NE Aegean), respectively to the E and W of a 45 km inland central portion. The 9 August 1912 Mürefte-Şarköy (M_s 7.4) and 13 September 1912 (M_s 6.8) earthquakes occurred along this segment. To date, the segment was studied mostly onshore although estimated magnitude and location suggest an offshore extension. Recent studies show the eastern rupture extension in the Sea of Marmara, while its western counterpart in the Gulf of Saros remains less documented. Here we use new observations from high-resolution marine geophysical data (multibeam bathymetry, side-scan-sonar, and seismic reflection profiles), to constrain the offshore 1912 ruptures in the Gulf of Saros. Detailed mapping of the subaqueous fine-scale morphology and structure of the fault provides a new insight for the western limit of the two 1912 surface ruptures. Distribution of fresh scarps, 3-D structural reconstructions, the complexity of fault segments, and the recent seismicity, altogether suggest that the western termination of the 1912 rupture(s) ends 37 km offshore in the Gulf of Saros. Following the 1999 Kocaeli earthquake, in the eastern Sea of Marmara, the unruptured segment length between the 1999 and 1912 ruptures became a critical issue, because of its implication for future earthquakes in the so-called Marmara seismic gap. If a 150–160 km total rupture length for the two 1912 earthquakes is assumed, a western rupture termination point at the inner Saros basin margin means that the eastern extension of the 9 August earthquake rupture reached the Central Marmara Basin. This outcome necessarily has implications for the seismic hazard in the Marmara coastal area that includes the Istanbul metropolitan area.

Key words: Earthquake hazards; Palaeoseismology; Continental tectonics: strike-slip and transform; Dynamics: seismotectonics; Submarine tectonics and volcanism.

1 INTRODUCTION

Mapping active faults in areas where inland tectonic structures extend offshore can be challenging. On such conditions, a precise assessment of a rupturing fault segment, which determines the potential maximum earthquake magnitude is difficult. A reliable hazard analysis requires a detailed fault map as a fundamental base, where geometrical fault complexities and related fault jogs (barriers) are determined. Well-documented surface ruptures of recent/historical earthquakes are a piece of supportive evidence that allows a better evaluation of the hazard. Tectonic-geomorphology and palaeoseismology are approaches that are widely used inland, for this purpose. Present-day marine geophysical technologies, dealing with the seafloor and subseafloor imaging, have reached resolutions and accuracies high enough to extend palaeoseismological methods and scales to the submerged environments (Polonia *et al.* 2002, 2004;

Armijo *et al.* 2005; McHugh *et al.* 2006; Gasperini *et al.* 2011a, 2018, 2021; Géli *et al.* 2021; Ribot *et al.* 2021; Uçarkuş *et al.* 2011; Yakupoğlu *et al.* 2019).

The 1600-km-long North Anatolian Fault (NAF) consists of complex fault geometries and traces of recent surface ruptures on both inland and offshore sections and provides a good opportunity to extend the well-established onshore palaeoseismic studies to the offshore. An important reason to seize this opportunity in this region is that the NAF below the Sea of Marmara is considered a seismic gap, to be filled by a large magnitude earthquake in the near future (Hubert-Ferrari *et al.* 2000; Parsons *et al.* 2000). This implies a high hazard to the nearly 20 million inhabitants of Istanbul and the heavily industrialized area around the Sea of Marmara. Here, in the Sea of Marmara, the NAF is segmented at different scales (Le Pichon *et al.* 2001; Armijo *et al.* 2005; Gasperini *et al.* 2021), and different scenarios regarding future earthquakes in this region are possible (Hubert-Ferrari *et al.* 2000; Parsons *et al.* 2000; Bohnhoff *et al.* 2013; Ergintav *et al.* 2014; Schmittbuhl *et al.* 2015; Lange *et al.* 2019; Meghraoui *et al.* 2021). A key point is determining accurately the maximum length of the Marmara seismic gap, which is delimited by the ruptures of the latest eastern (1999 Kocaeli) and western (1912 Mürefte-Şarköy) earthquakes. The total length of the 1999 Kocaeli earthquake and its offshore extension in the Sea of Marmara is well established (Barka *et al.* 2002; Uçarkuş *et al.* 2011; Gasperini *et al.* 2011a; Çakır *et al.* 2003). However, the total length of the 1912 earthquake is less constrained. because only a 45-km-long section of the NAF is located inland. The inland surface ruptures of the 9 August 1912 Mürefte earthquake (M_w: 7.4) related coseismic offsets of up to 5.5 m are documented in earlier studies (Mihailovic 1927; Ambraseys & Finkel 1987; Altınok *et al.* 2003; Altunel *et al.* 2004; Aksoy *et al.* 2010; Aksoy 2021). The destructive earthquake was followed by a second large shock of M_s 6.8 on 13 September 1912 that occurred further west and caused noteworthy damage in the region (Ambraseys & Finkel 1987; Aksoy *et al.* 2010). The ruptured segments in the Gulf of Saros and the total rupture dimensions of these two earthquakes are controlled by the local tectonic structures and by the moment magnitude of the earthquakes. Therefore determining the western endpoint of the ruptures allows estimating an eastern tip for the 9 August 1912 rupture and hence has implications in evaluating the size of the seismic gap in the Sea of Marmara.

This study presents new observations from high accuracy multibeam bathymetric data, high-resolution seafloor images (side-scan-sonar), and shallow subsurface data (CHIRP) for the offshore continuation of the NAF in the Gulf of Saros. The new observations allowed us to reappraise the location and dimension of the offshore sections of the 9 August and 13 September 1912 surface ruptures.

2 THE NAF AND ITS WESTERN SEGMENTS

The NAF is the largest and most active strike-slip fault system in the Mediterranean region. The right-lateral transform boundary fault is a product of the post-collisional convergence of Eurasia and Arabia and accommodates the westward escape of the Anatolian block at a rate of 24 mm yr^{-1} (McKenzie 1972; Reilinger *et al.* 2006). The westward motion is accompanied by an anticlockwise rotation due to the backward retreat of the Hellenic slab (Armijo *et al.* 1999; Chorowicz *et al.* 1999; Philippon *et al.* 2014) which results in a widespread extension in the Aegean and western Turkey (McKenzie 1972). The shear zone of the NAF widens from east to west. In the Marmara region, it divides into two main branches (Fig. 1, Barka & Kadinsky-Cade 1988; Armijo *et al.* 1999). The northern branch in the Sea of Marmara is the most active one and is associated with several secondary normal faults and deep basins (LePichon *et al.* 2001; Armijo *et al.* 2005; Şengör *et al.* 2005; Gasperini *et al.* 2021). Further west, the northern NAF is exposed inland for 45 km as a linear narrow strike-slip deformation zone (Ganos fault) and widens westwards in the Gulf of Saros with two main splays (Fig. 2a, Kurt *et al.* 2000; Okay *et al.* 2004; Ustaömer *et al.* 2008; Aksoy *et al.* 2010; Gasperini *et al.* 2011b).

The 45-km-long inland section of the Ganos fault is a narrow linear valley less than 1.5 km wide and trends N70°E (Fig. 2a). Deformation is localized and well expressed by typical morphological structures of strike-slip faulting (e.g. pressure ridges, shutter ridges, stream offsets, step-overs with right or left stepping jogs, releasing and restraining bends, back-tilted slopes and sag-ponds). Locally, 1–10 m high-scarps signify the vertical component of the fault. The linear fault geometry is continuous and extends offshore into the Gulf of Saros (Fig. 2b). The 1912 surface ruptures along the Ganos fault have been well documented through contemporary photographs, recent field investigation and trenching studies (Mihailovic 1927; Ambraseys & Finkel 1987; Rockwell *et al.* 2001, 2009; Altunel *et al.* 2004; Meghraoui *et al.* 2012; Aksoy 2021).

The detailed mapping of surface ruptures is an essential task for determining the dimensions of seismic gaps in neighboring fault segments. On the NAF, a westward propagating sequence of eight earthquakes from 1939 to 1999 ruptured nearly an 1100-km-long section of the fault. The associated surface ruptures are well documented in earlier studies (Pamir & Ketin 1941; Ambraseys & Zapotek 1969; Ambraseys 1970; Barka & Kandinsky-Cade 1988; Barka 1996, Akyüz *et al.* 2002; Aydın & Kalafat 2002; Barka *et al.* 2002; Langridge *et al.* 2002; Rockwell *et al.* 2002; Kondo *et al.* 2005; Emre *et al.* 2020). The 17 August 1999 (M_w 7.4) earthquake rupture extends offshore towards the east of the Sea of Marmara until the eastern limit of the Çınarcık basin and represents the western tip of the sequence (Fig. 1; Uçarkuş *et al.* 2011; Gasperini *et al.* 2011a). The 9 August 1912 Mürefte-Şarköy earthquake (M_w 7.4) occurred west of the Sea of Marmara, along the Ganos fault segment. The rupture broke the 45-km-long inland section and stretched out into both directions; towards the Sea of Marmara and the Gulf of Saros (Fig. 1). Field observations and palaeoseismic trenches document 5.5-m-right lateral displacement at Güzelköy; located 5.8 km west of the Marmara coastline (Altunel *et al.* 2004; Meghraoui *et al.* 2012). Offshore studies in the Sea of Marmara contribute to these observations providing evidence of fresh submarine earthquake scarps and homogenite deposition in the Ganos basin related to the 1912 earthquake (Armijo *et al.* 2005; McHugh *et al.* 2006; Drab *et al*. 2012). In trenches near the coast of Saros, Rockwell *et al.* (2001, 2009) determined ruptures related to the 1912 event and calculated 4.5 m lateral coseismic displacement that suggests an offshore rupture continuation (Fig. 2). Earlier studies estimated 56–160 km total rupture length for the 9 August shock (M_w 7.4, Ambraseys & Jackson 2000; Altınok *et al.* 2003; Le Pichon *et al.* 2003; Altunel *et al.* 2004; Armijo *et al.* 2005; Karabulut *et al.* 2006; Aksoy *et al.* 2010; Aksoy 2021). These estimations are based on field observations and fault scale relationships using the earthquake magnitude. Altınok *et al.* (2003) suggested a 56 km length for the 9 August rupture with its western limit at Kavak and eastern limit

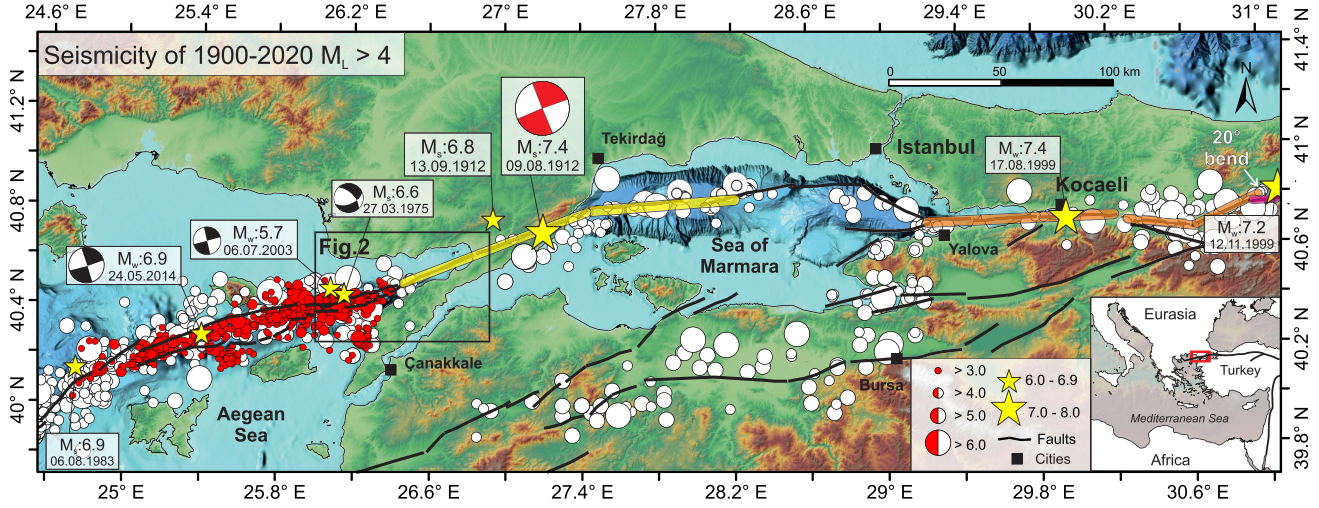

Figure 1. The North Anatolian Fault in the Sea of Marmara and the Gulf of Saros experienced several large earthquakes in the last century (yellow stars). The white circles show the seismicity from 1900 to 2020 for $M_L > 3$ events (source KOERI 2020). East of the Sea of Marmara, the two earthquakes in 1999 (M_w 7.4 and 7.2) are the most recent destructive earthquakes of NAF. 17 August 1999 event, produced a bilateral rupture that extended into the Sea of Marmara, reaching the Çınarcık basin (Uçarkuş *et al.* 2011; Gasperini *et al.* 2011a). On the West, the 9 August 1912 (M_s 7.4), 13 September 1912 (M_s 6.8), 1975 (M_s 6.6), 1983 (M_s 6.9) and 2014 (M_w 6.9) earthquakes are other potentially surface rupturing events along the western main branch of the NAF. The ruptures of the 17 August 1999 (orange stripe) and the 9 August 1912 (yellow strip) form the seismic gap of the Sea of Marmara (Armijo *et al.* 2005; Aksoy *et al.* 2010). Location and focal mechanism solution for 1912 events are from Ambraseys & Jackson (2000) and Aksoy *et al.* (2010) respectively. Other solutions for the 1975 earthquake are from Taymaz *et al.* (1991), the 2003 earthquake from Karabulut *et al.* (2006), the 2014 earthquake from Konca *et al.* (2018). The red circles highlight the 24.05.2014 earthquake seismic sequence from May 2014 to October 2014 (earthquakes are from EMSC 2020). The eastern limit of the earthquake swarm coincides with the major bifurcation of the NAF in the Saros Gulf (image modified from Aksoy 2021).. I

north of the Tekirdağ basin. A similar eastern endpoint has been proposed by Le Pichon *et al.* (2003) with an uncertain western extension into the Gulf of Saros. Considering the offshore observations in the Tekirdağ and Central basins Armijo *et al.* (2005) estimated a rupture length at least 110-km long and possibly up to 140 km if extended into the Gulf of Saros. Aksoy *et al.* (2010) calculated a total length of 120± 30 km for the 9 August rupture combining the fault geometry, the earthquake magnitude (M_w 7.4), slip distribution (4–5 m at east and west of the inland section), and source duration (40 s) and estimated that a 40-km-long rupture section lies in the Gulf of Saros (of the 9 August and 13 September shocks). The wide range of suggested rupture lengths and variety of termination points leave the offshore extension of the 1912 rupture a matter of debate, particularly in the Gulf of Saros.

3 DATA AND METHODS

We collected high-resolution multibeam bathymetry, shallow-penetration seismic reflection, and side-scan-sonar data onboard of the R/V Urania of the Italian CNR (Consiglio Nazionale delle Ricerche) during two cruises, in 2005 and 2011 (see cruise reports for more details at http://ricerca.ismar.cnr.it/CRUISE_REPORTS/SRC/ISMAR-BO/). The 2005 cruise surveyed the deeper sectors of the Saros basin through 5- to 20-km-long NW–SE trending transects between longitudes 26° to 26.7° (Fig. 2b). The cruise in 2011 overlapped the eastern part of the 2005 cruise and surveyed the remaining shallower parts of the basin, between longitudes 26.5° to 26.8°. All data were positioned using a DGPS (Differential Global Positioning System) and SEAPATH (Position, Attitude, Time and Heading) system, and were corrected for offsets between the GPS antenna and different transducers using gyrocompass and CMG data. Positioning errors were within ±1 m. In the 2011 cruise, the swath bathymetry was collected with a Kongsberg EM 170 Multibeam echo sounder (70 kHz, 400 1 × 2°, 150° aperture, 2000 m range). The high-resolution seismic reflection data were collected with 16 transducers Teledyne-Datasonics Chirp III Acoustic Profiling System, and a 1 kJ Geo-Source 1600 Ocean Depth Multi-Tip Sparker System. We also tracked the fault with EdgeTech 4200 FS Sidescan Sonar System (100/400 kHz) to reveal further details on potential surface ruptures. The side-scan sonar data were mosaicked using SwanMosaic 2.0 of the Communication-Technology company (Cesena, Italy). The multibeam data uncertainties are depth-dependent, ranging from 1 to 2 m in shallow waters to over 6 m in deeper parts of the basin. The sub-seafloor images of the CHIRP data were obtained using the open-source software package SeisPrho (Gasperini & Stanghellini 2009). The collected data of the 2011 cruise were combined with existing data from the 2005 cruise; for details see Gasperini *et al.* (2011b) or the associated cruise report in the repository link given above.

The seafloor bathymetry map has been constructed using a similar tectono-morphic approach as applied in inland fault sections. The 2-D digital fault map has been prepared simultaneously with subseafloor images and therefore provides a 3-D examination of the fault structure (Fig. 2b).

Using the bathymetric map, side-scan-sonar images, and high-resolution seismic data, we investigate the surface morphology and fault geometry in 3-D for the superficial section of the NAF. Combining these new observations with earlier crustal-scale analysis and recent seismicity we discuss the possible rupture barriers along the Saros-Ganos fault and suggest a western endpoint for the 1912 earthquake ruptures.

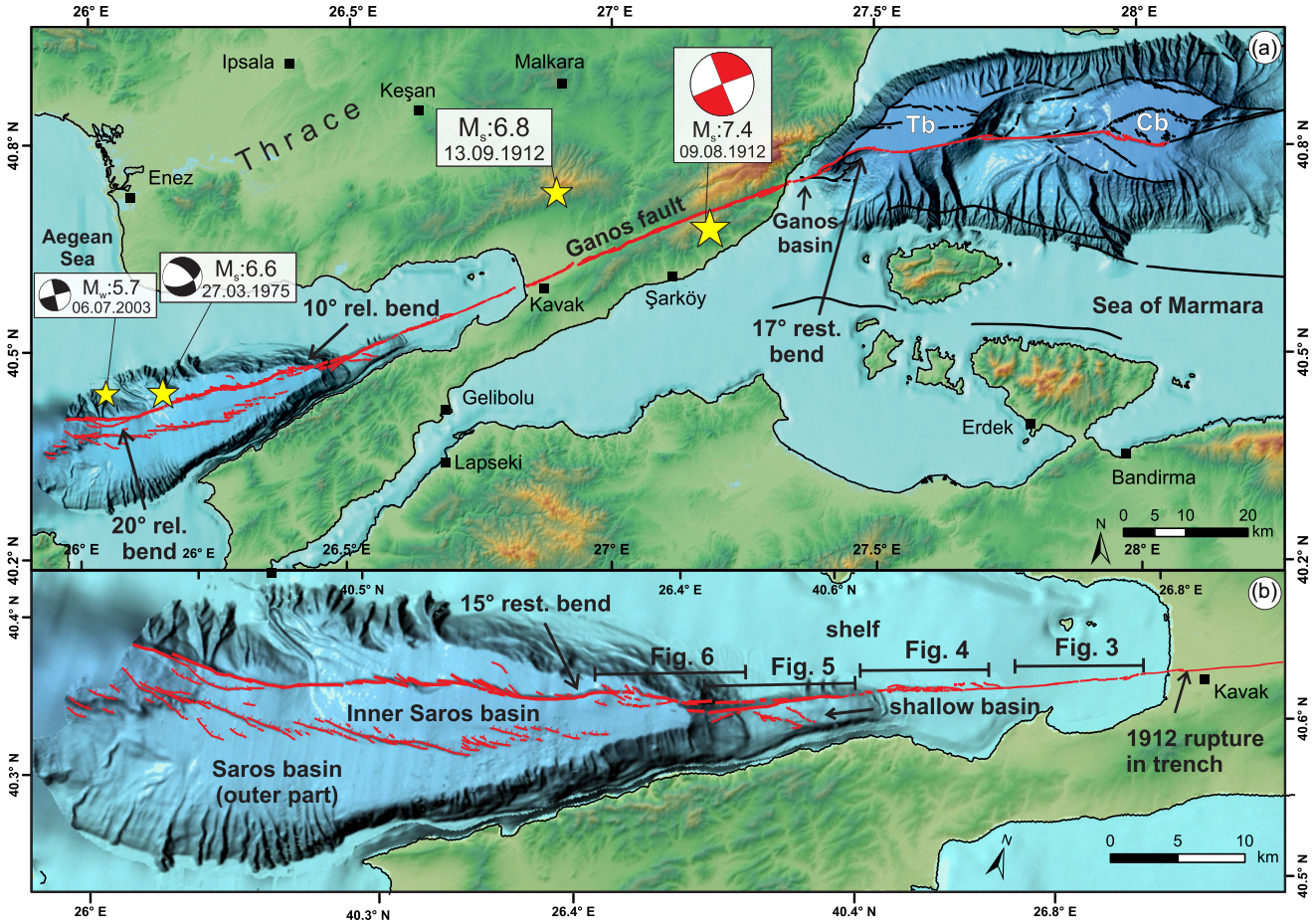

Figure 2. (a) The NAF in the Sea of Marmara crosses the central basin (Cb) and the Tekirdağ basin (Tb). The westernmost inland section of the NAF (red lines) forms a very linear geometry with minor step-over areas creating sagponds and pressure ridges. Surface ruptures have been exposed during palaeoseismic trenching campaigns near the coast of the Gulf of Saros. Rockwell *et al.* (2001, 2009) revealed two surface rupturing events dating post AD 1655, and attributed them to the 1766 and 1912 earthquakes, and suggested 4–5 m coseismic slip for each event based on a 9 ± 1 m displaced feeder channel thalweg. (b) The offshore section of the NAF (red lines) has been studied during the R/V Urania MARMARA-2005 and -2009 cruises and a 15 m resolution swath bathymetry was collected. The offshore fault geometry is rectilinear on the shelf section, with minor step-overs. Towards the deeper section of the Saros basin, the fault increases in complexity and bifurcates into two sections. The southern strand consists of several trans-tensional faults forming scarps oriented in an en-echelon array. The northern strand consists of a ∼60-m-high continuous morphological escarpment produced by a rectilinear main fault.

4 RESULTS

4.1 Seafloor morphology of the Gulf of Saros

The Gulf of Saros lies between the Thrace and Gelibolu Peninsulas and forms the easternmost section of the North Aegean Trough (Figs 1 and 2). In map view, the Gulf basin has an elongated triangular shape that widens and deepens to the west. It is asymmetric with its longitudinal axis trending SW–NE. Bathymetrically the Gulf area consists of (1) a wide shelf area extending to −125 m (in the north and east), (2) a −200-m-deep transitional basin in the east and (3) the main Saros basin with depths of −550 to 700 m (Fig. 2). The Saros basin has a steep (15–70°) southern margin. The northern margin connecting the wide shelf with the deep basin has slopes of 5–25°. The slopes are cut by canyons and erosional gullies. (Figs 2 and 5). The deep basin is subdivided into an outer and inner basin by 50–100-m-high escarpments at the north and south. The northern escarpment is a single 40-km-long continuous structure with minor steps and jogs. The scarps at the south are less steep, exhibit an en-echelon and staircase geometry and reach cumulatively the same height.

4.2 The NAF in the Gulf of Saros

In earlier studies, the NAF in the Gulf of Saros has been mapped as a single fault in the shelf and forming a splay towards the deeper section, where two fault branches follow the northern and southern basin margins (Tüysüz *et al.* 1998; Kurt *et al.* 2000). However, Ustaömer *et al.* (2008) show that the current transtensional deformation is concentrated along the central section of the gulf.

4.2.1 The shelf area

In the shelf, the NAF is a single through-going strike-slip fault (Ustaömer *et al.* 2008). Our new improved bathymetric data exposes more details (Figs 3–6). In the eastern shelf section, the NAF is visible as a 12-km-long linear single escarpment striking

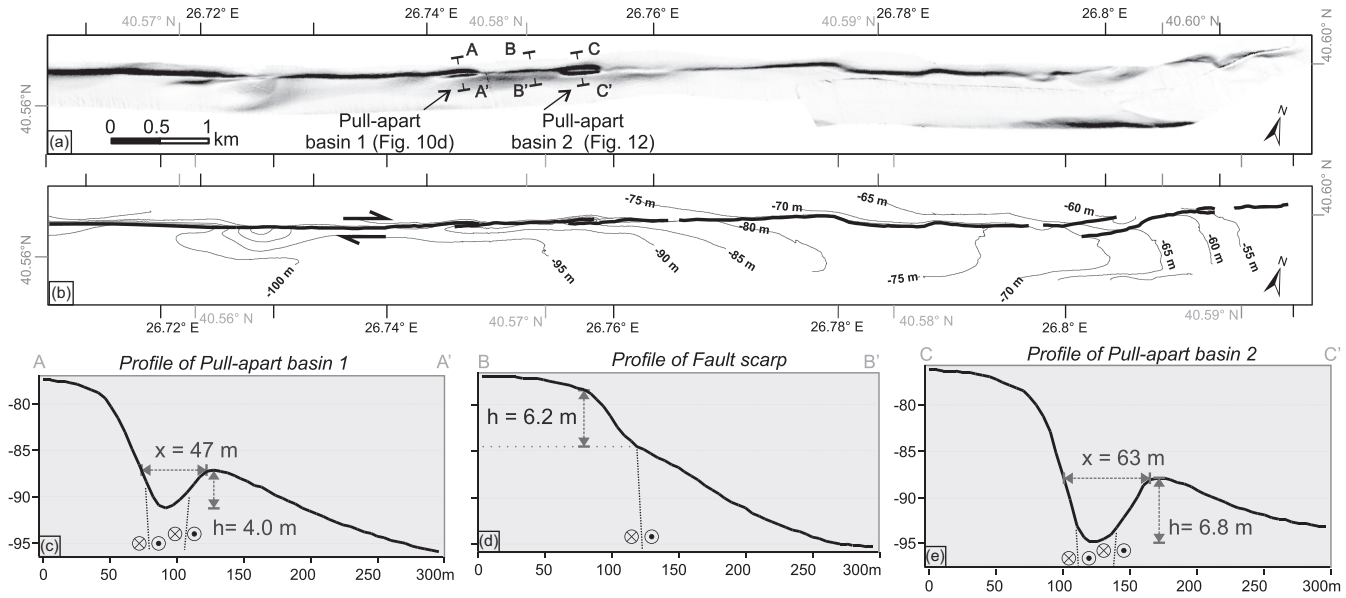

Figure 3. (a) DEM of the multibeam survey, illuminated from SW (North is rotated 18°). (b) Fault map with 5 m interval bathymetry contours. Here the NAF on the shelf section is visible as a very linear sharp escarpment with minor complexities. For map locations see Fig. 2(b). The height of the escarpments vary along strike however increases towards west. On the topographic profile B–B' the scarp height is measured as 6.2 m. Section A–A' and C–C' show bathymetry profiles across the two pull-apart basins.

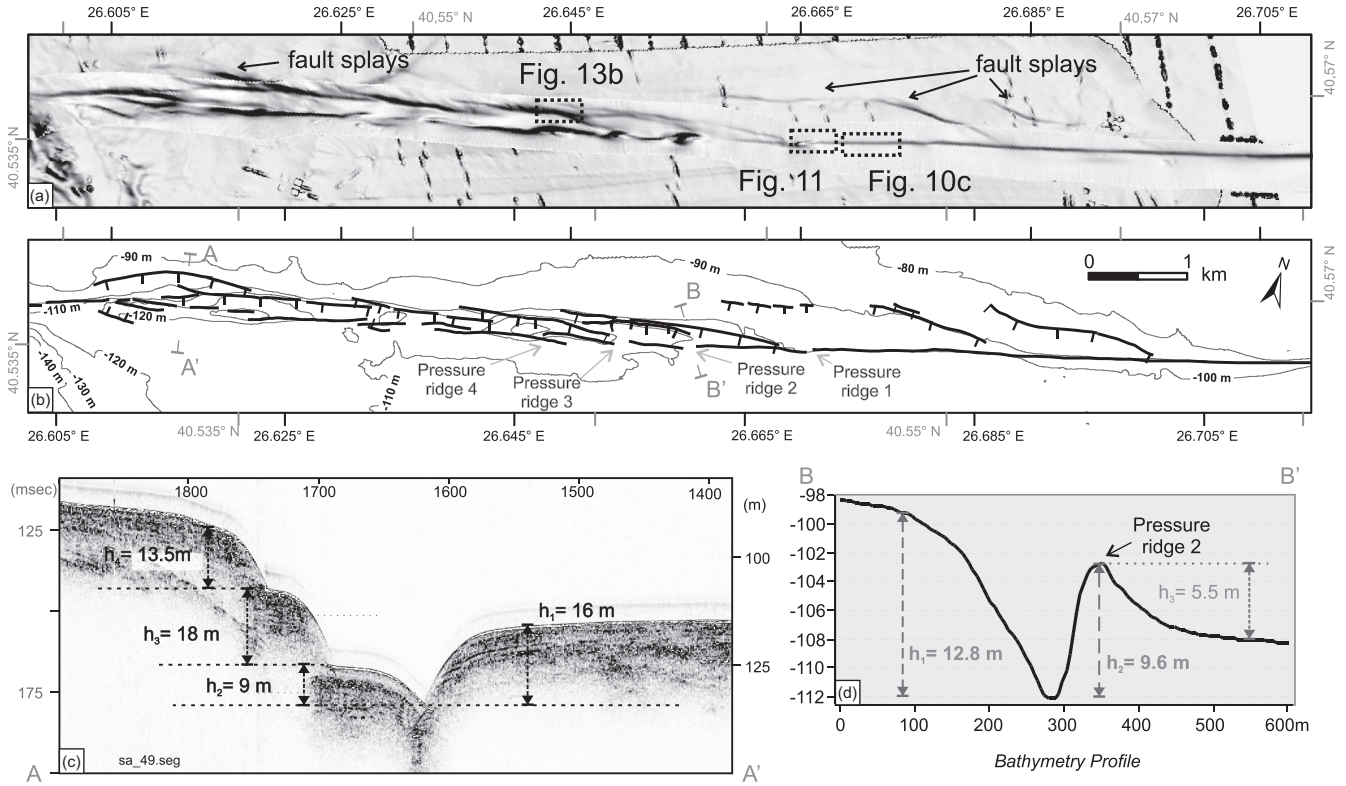

Figure 4. (a) DEM of the multibeam survey, illuminated from ~E (north is rotated 18°). (b) Fault map with 10 m interval bathymetry contours. Westwards the fault bifurcates into two splays forming a 7-km-long, linear, narrow, shallow basin, which is approximately 200 m at its widest part. For map locations see Fig. 2(b). The water depth varies from −110 to −130 m along its long axis. The northern splay is formed by 1- to 2-km-long trans-tensional faults in a left-stepping array (a, b). The southern limit however is bounded by a single fault. The southern splay faults are shorter (<1 km) and show an en-echelon orientation (b, c). Several pressure-ridges along the southern branch also testify a dominant strike-slip deformation. The height of the ridges ranges between 1 and 5.5 m and could be attributed to the coseismic deformation of probably 1–3 earthquakes (b, d). (c) The CHIRP profile A–A' shows several normal faults on the north with a scarp height of 9–18 m (Table 1).

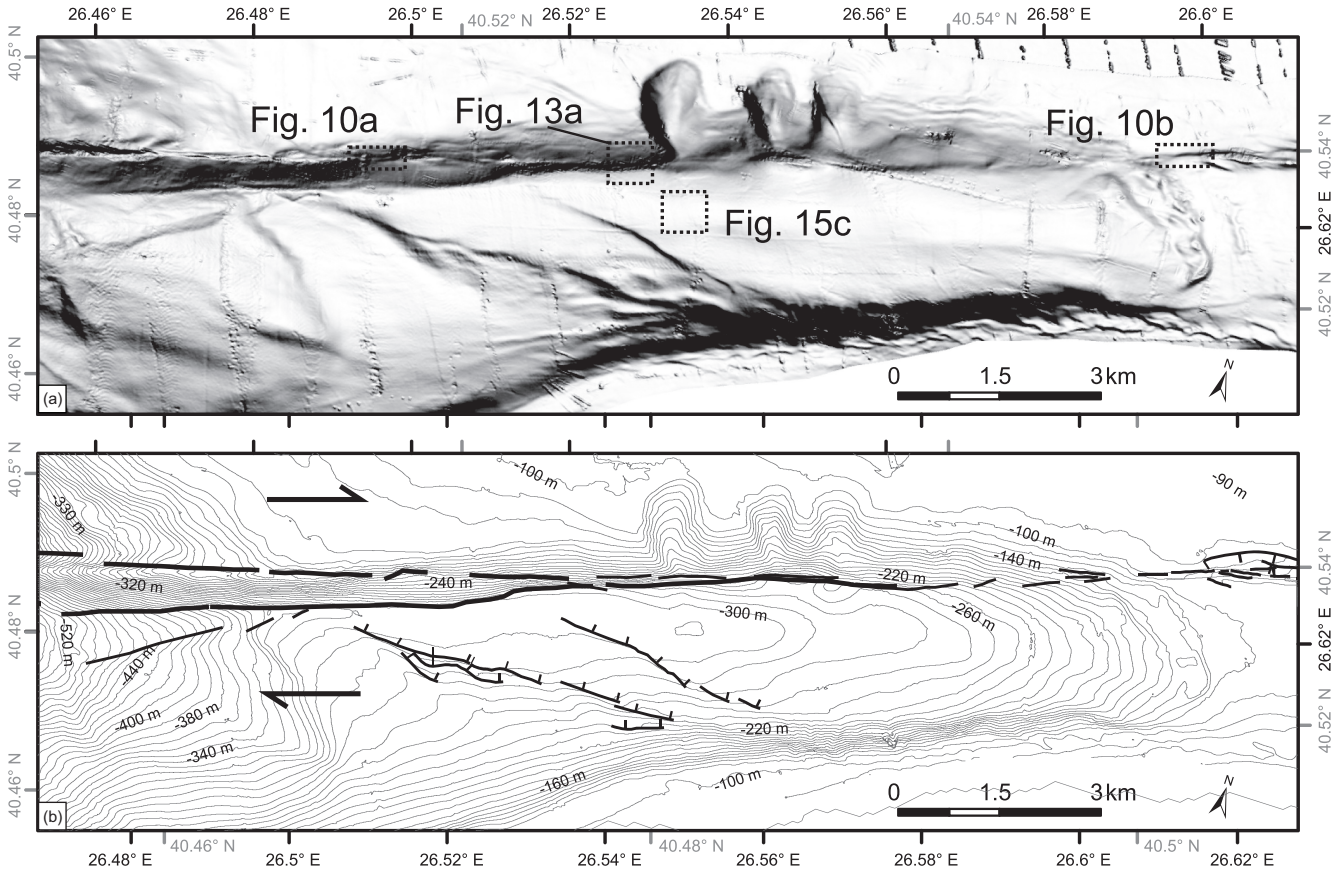

Figure 5. (a) DEM of the multibeam survey, illuminated from ~SW (north is rotated 18°). (b) Fault map with 10 m interval bathymetry contours. Here, the shelf deepens abruptly from −100 m to approximately −300 m and opens towards a 42-km-wide and 10-km-long basin. The NAF runs WSW as a linear structure along the northern margin of the basin. On the south, ESE trending antithetic trans-tensional faults contribute to the deformation. For the map location see Fig. 2(b).

247 ± 2° with minor geometrical changes along the strike (Fig. 3). The general height of the SE facing escarpment is 8 to 9 m and increases westwards up to 16 m. Faulting is limited within a zone of 100–300 m wide (Fig. 3). There are two significant dilatational fault jogs along this section of the fault. In map view, the size of the fault step in sagpond-like basin-1 and basin-2 is 30 and 40 m, respectively. Both basins are approximately 400 m in length with a depth of 4–7 m. Towards west, splays widen the deformation zone to ~1000 m and form a 5-km-long linear depression (Fig. 4). The splays are 1- to 2-km-long normal faults dipping S–SW and constitute the northern margin of the depression. They diverge in the NW direction, form a left bend, and become parallel to the main fault. Individually, the throw on each fault varies from 4 to 18 m and form collectively a 40-m-high scarp in a stair-case geometry (Table 1). The seismic (CHIRP) profile in Fig. 4(c) exposes the vertical displacement of Quaternary deposits and the fault geometry towards depth. The southern margin however is a 10- to 16-m-high single escarpment. An elevation difference of 10–30 m is notable between the northern and southern basin flanks suggesting that the southern margin fault is contributing to the subsidence in the long-term. This is also evident in the seismic reflection profile where the uppermost sedimentary deposits in the central basin show tilting towards the southern fault (Fig. 4c). Conversely, the up to 5.5-m-high pressure-ridges along the southern margin shoulder manifest the dominant strike-slip deformation on the margin fault. In map view, the width of the left step-overs is 60–80 m.

4.2.2 The shallow transitional basin

Further west, at approximately 125 m depth, the shelf morphology shows a transition to the 3- to 4-km-wide and 10-km-long intermediate basin that reaches a depth of 310 m (Fig. 5). Its northern margin is a single steep escarpment along which the NAF strikes 250 ± 2° as a single fault with minor step-overs. The basin is asymmetric with a floor tilted towards the fault (north). The high-resolution multibeam bathymetry exposes two NW-striking escarpments on the SW end of the basin. These 15-m-high scarps are ESE-trending antithetic oblique faults that contribute to the transtensional deformation. Considering the orientation of the faults and the slope morphology, the bathymetry contours bend rightwards across the fault signifying a right-lateral strike-slip component. On the northern margin, three distinct canyons entrench the northern slope morphology. The submarine canyons fronts are truncated by the fault. The NAF bifurcates into two strands at the western limit of the basin where two antithetic normal faults develop. The main NAF runs parallel along the two flanks of a 5-km-long and 500-m-wide linear ridge.

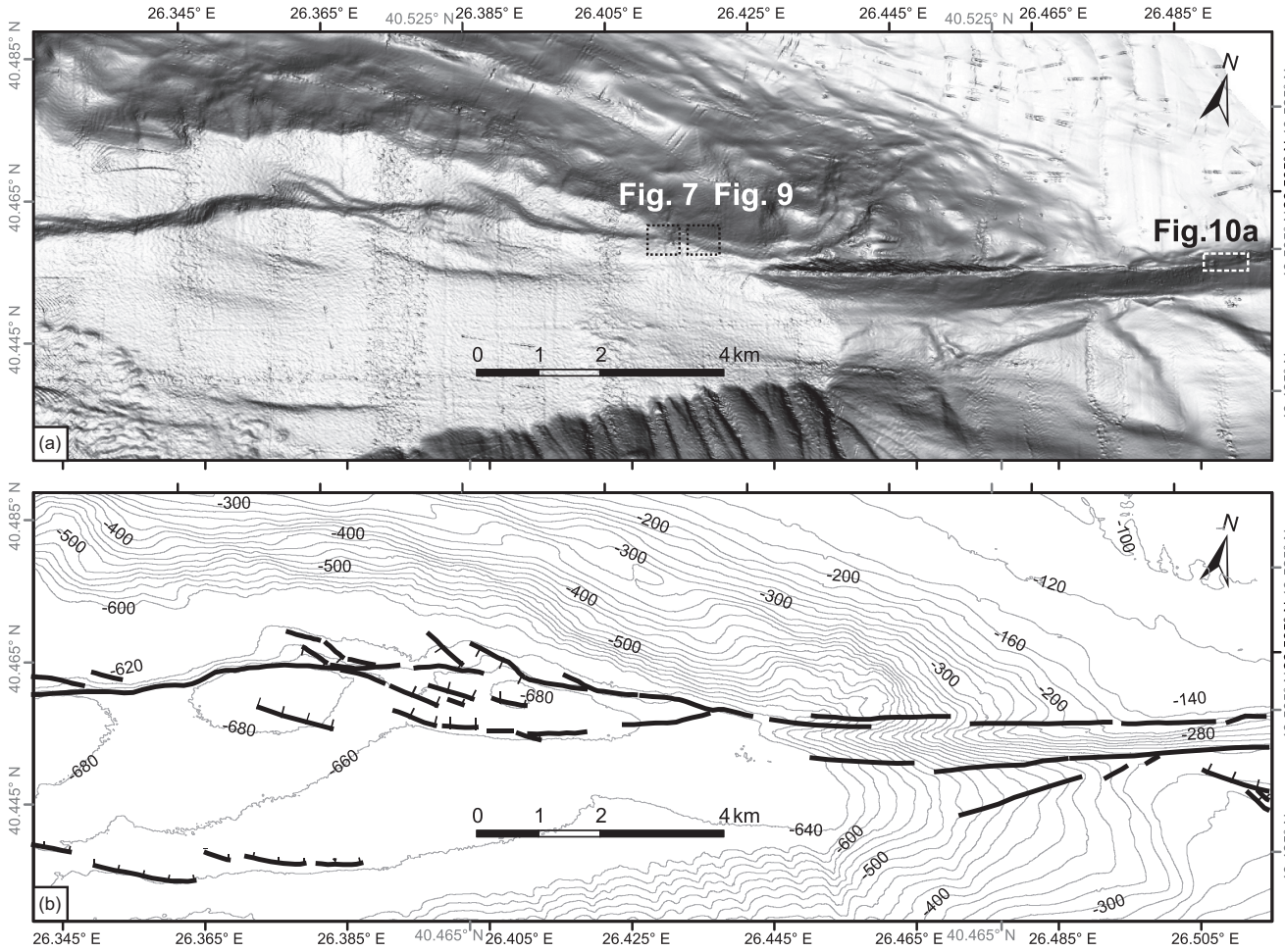

Figure 6. (a) DEM of the multibeam survey, illuminated from ∼SW (north is rotated 15°). (b) The Saros basin is marked on its eastern margin by an abrupt change in depth from approximately −300 to −650 m depth. The N–S margins of the deepest part of the Saros basin are controlled by left-stepping trans-tensional faults on the south, and a dominant strike-slip deformation on the north. Right-laterally offset structures have been documented along this section (Gasperini *et al.* 2011b).

Table 1. List of offset measurements.

Name	Offset	Error	Type (throw or right lateral slip)	Fig.
Ridge	24		right lateral slip	11
Scarp	13.5		Throw	4
Scarp	18		Throw	4
Scarp	9		Throw	4
Scarp	10.2	±0.2	Throw	8
Scarp	4.3	±0.2	Throw	8
Scarp	1	±0.2	Throw	8

A few kilometres west, the southern fault bifurcates again with an SW striking (238°) 3-km-long fault.

4.2.3 Inner Saros basin

The main Saros basin shows a basin-in-basin morphology, where the inner basin is embraced by strike-slip and normal faults. In general, the strike-slip deformation runs along the northern margin of the inner basin and involves a significant amount of normal component evident by the ∼60-m-high continuous escarpment. The southern basin margin is composed of WNW-striking normal faults that are oriented en-echelon and form a staircase morphology (Fig. 6). Where the NAF enters the basin (East), the fault geometry becomes more complex, with 1 to 4-km-long splays striking NW and WSW. It makes a significant 10° bend to the right (releasing bend) and veers again 15° left (restraining bend) forming an arcuate fault geometry (Fig. 2). The area within this arc geometry is subsiding, controlled by trans-tensional deformation on the north and normal faults in the south. The small basin is 4 km by 900 m in size (Fig. 6). Further west, the fault forms a continuous sinusoidal single escarpment that extends for 30 km. The complexity of the fault is limited. Small (1–3 km) splays striking WNW and left stepovers with a maximum 500-m-width contribute to the strike-slip deformation (Fig. 2). Gasperini *et al.* (2011b) measured 130 ± 10 m right-lateral displacement of a canyon along this section of the fault.

4.3 Seafloor expressions of the recent faulting events

One of the targets of the 2011 Urania cruise was to search for possible fresh fault scarps that could be associated with the 9 August and 13 September 1912 earthquakes. Aksoy *et al.* (2010) approximated the western rupture termination of the 1912 earthquakes to be 40 km offshore from the eastern coastline in Kavak. This corresponds to the

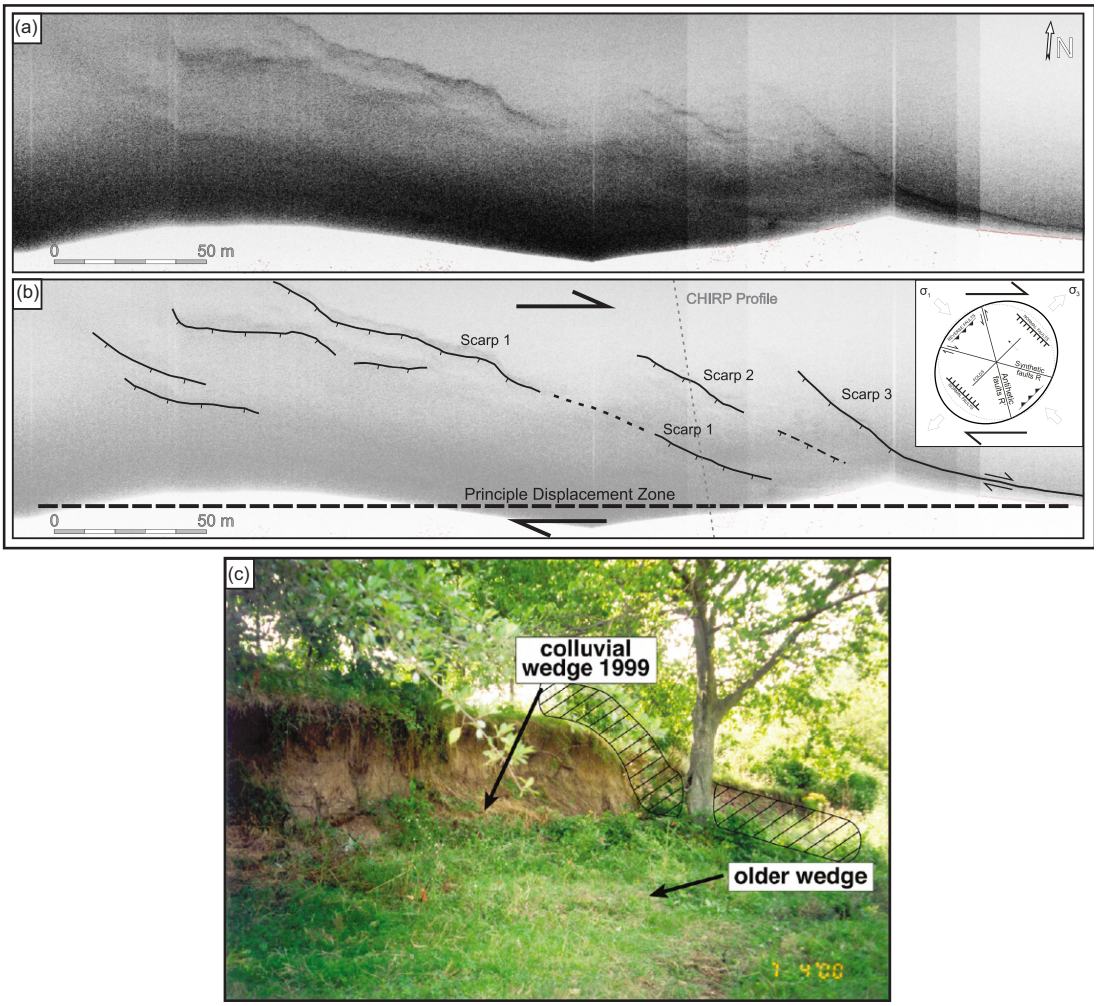

Figure 7. (a) Side-scan sonar image from the deeper section of the Saros basin (see Fig. 6 for location). The dark areas indicate high backscatter from south facing steep slopes. (b) Structural interpretation of the sonar image in (a) shows an array of left and right stepping fresh fault scarps. These NW striking trans-tensional faults are splay faults of the NAF. (c) Analogous splays and scarps that occurred inland during the 17 August 1999 earthquake (photo: Klinger *et al.* 2003)

eastern limit of the inner Saros basin (Fig. 2). The estimation is based on the fault geometry (detailed inland but rough offshore map), the inland slip distribution, the seismic moment, and the rupture duration for the 9 August shock. The previous offshore fault analysis has been carried out using the low-resolution bathymetry map of Ustaömer *et al.* (2008). In the present study, we used high-resolution multibeam-bathymetry, together with side-scan-sonar data to examine the offshore extension of the 1912 surface ruptures. Our survey starts 2 km west of the termination point proposed by Aksoy *et al.* (2010) and continued eastwards until 750 m offshore of the Kavak coast. The entire sonar survey covers a 37-km-long sections of the NAF with a swath width of 200 m.

A smooth inclined seafloor surface at the northeastern inner basin boundary is shown in Fig. 7. The floor is interrupted by en-echelon scarps. The strong reflections (dark) on the image expose steep scarp faces. The faces have well-preserved crest lines which in map view show a sinusoidal geometry. The baseline of the scarps correspond to faults, oriented NW–SE with a clockwise angle of 20–40° to the principal displacement zone. The downthrown hanging-wall surface is identifiable on scarp 1 as a planar surfgace at the base of the scarp; which likely represents the actual throw. On scarp 2 and 3 the throw is less distinct because the scarps are buried with sediments deriving from the higher parts of the slope. Although the scarp heights are not measurable from the side-scan-sonar, a nearly orthogonal CHIRP profile at the site allows an approximation. The sub-bottom section in Fig. 8 shows a smooth basin floor topography with a depression in the centre and scarps towards the north. The main branch of NAF is visible as a wedge-shaped acoustic reflectivity region below the central depression. In the south, a 5-m-thick (Holocene) layer overlays a well stratified subhorizontal sequence. A similar stratigraphy has been described further west in the Aegean Trough where the uppermost high amplitude reflectors (green, yellow, turquoise) have been considered to represent the last glacial–interglacial transgression at ∼16–18 ka (McNeil *et al.* 2004). All the units are folded and interrupted by the NAF. The folded succession signifies the compressive lateral component of the strike-slip deformation. The scarp 2 in the sonar data (Fig. 7) corresponds to the northernmost scarp in the sub-bottom profile (Fig. 8). Taking the southernmost horizontal seafloor as reference the total height of the scarp is 10.2 ± 0.2 m (h_3).

A second scarp further south measures 4.3 ± 0.2 m vertical displacement. The central depression is 1 ± 0.2 m deep. Other

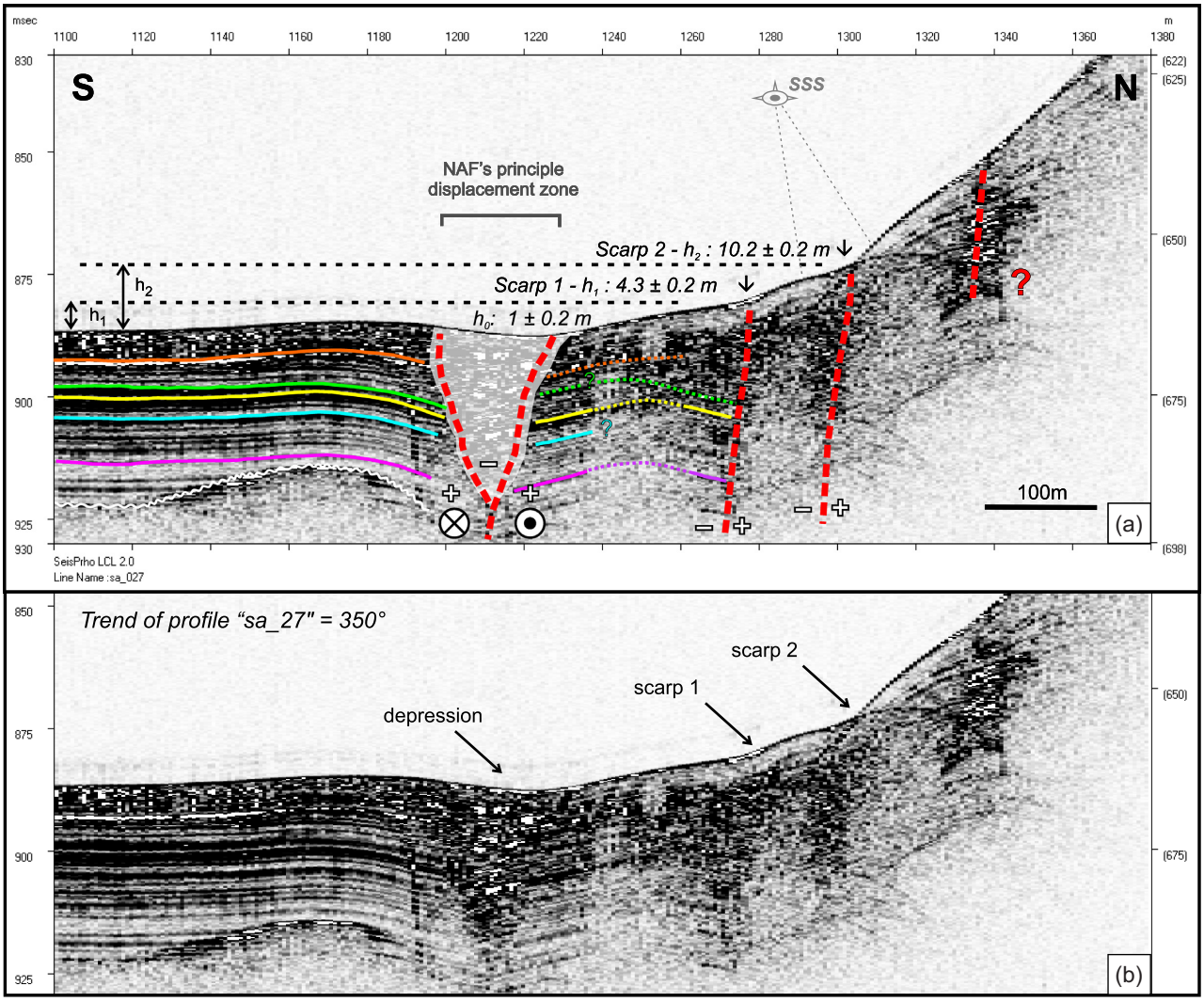

Figure 8. (a) A CHIRP profile that crosses orthogonally the scarps observed in Fig. 7. Dashed red lines indicate active faults. Other colored lines mark significant reflection horizons of Quaternary deposits. The deformed structure of the layers implies a compressional deformation. The movement of the blocks is marked as ⊗away from the reader, ⊙ towards the reader. We measured a total scarp height of 10.2 ± 0.2 m and a second cumulative scarp of 4.3 ± 0.2 m (Table 1). In cooperation with the 1 m depression at the central faults, these structures mark the displacement of recent faulting events. (b) Is the uninterpreted version of the CHIRP profile.

scarps with high reflectivity are visible a few hundred meters east from Fig. 7 (Fig. 9). Here, the NAF is observed as a network of fractures that is 37-m-wide and 400-m-long. The anastomosing fracture geometry is characteristic of strike-slip faulting. A visual comparison of the scarps in Figs 7 and 9, suggests that these scarps are likely less than 5 m high. The high reflectivity indicates steep scarp faces which implies the scarps experienced no or little erosion and therefore likely represent the actual throw.

Fig. 10 illustrates similar scarps along the eastward fault section. Two linear structures at the western and eastern tips of the intermediate basin indicate recent faulting localized in a very narrow (<1 m) deformation zone. Both faults run subparallel along a southward-facing slope. The western lineament appears fresh and well preserved, while the eastern fault is partially covered with sediments (Figs 10a and b). Along the shelf, a 7–10-m-high escarpment is accompanied by a sharp, distinct lineament along the scarp base. The structure is 0.5–1.5 m wide and can be traced continuously for 8 km along the shelf (Fig. 10c). Considering the total scarp height, this individual scarp is likely less than 1-m-high. Eastwards, the fault is less distinct, nevertheless, two fault jogs forming depressions mark the young tectonic activity (Figs 10d and 12). Fresh tectonics structures are identifiable along the entire 37-km-long surveyed section. They are well preserved at regions with less sediment input and become less distinct eastwards because of increasing sediment input approaching the mouth of the Kavak river (Çağatay *et al.* 1998).

The sonar study allowed us to determine additional structures that manifest the right-lateral strike-slip deformation in the Saros basin. In the shelf area, where the deformation is localized on the main branch fault we determine a truncated ridge morphology (see Fig. 4 for location). The fault scarp in the acoustic image is evident by a strong linear reflector (Fig. 11). The hill slopes are visible as dark areas and are noticeably truncated by the fault (Fig. 11b). A reconstruction of the lateral slip allowed to measure a displacement of 24 m. The lateral offset signifies the cumulative strike-slip

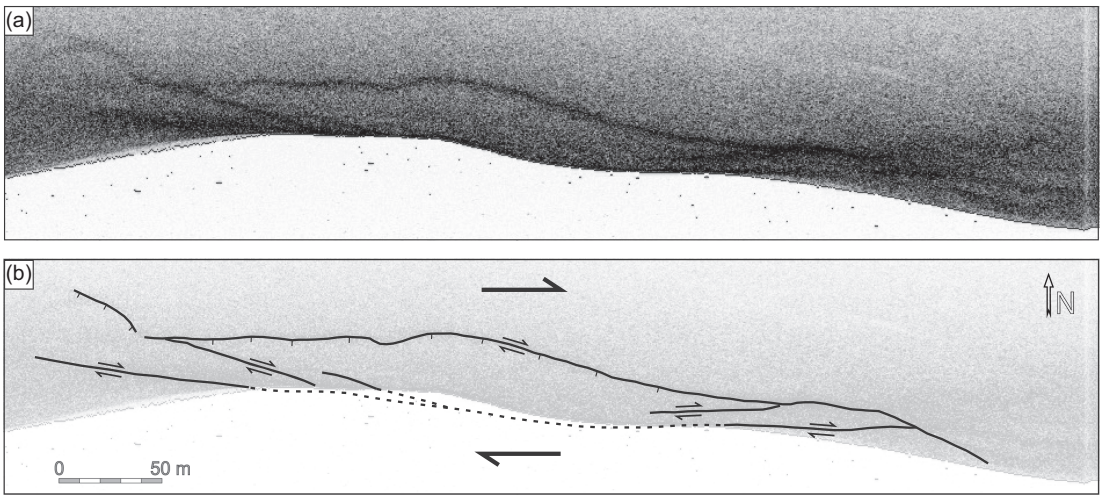

Figure 9. (a) A side-scan sonar image from the deeper section of the Saros basin (see Fig. 6 for location). (b) E–W striking fresh scarps form an anastomosing geometry (profile: SAR_SS01H). For location see Fig. 6.

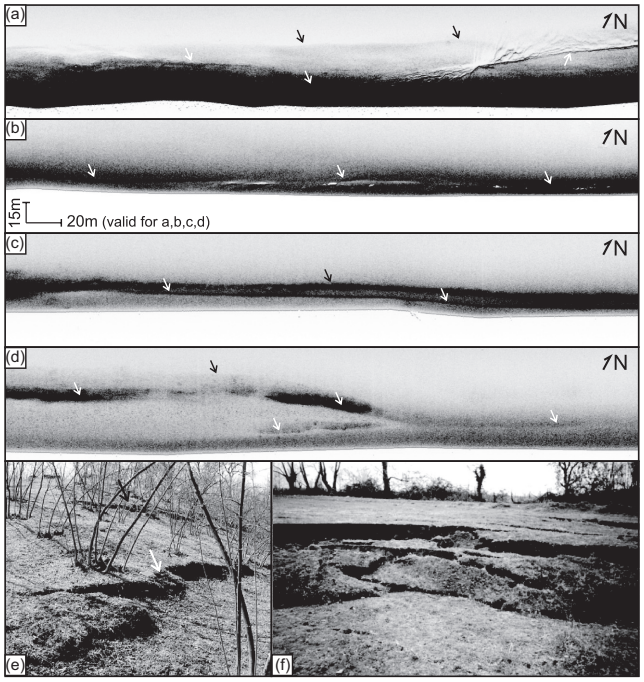

Figure 10. Side-scan sonar (SSS) images from several locations along the 37-km-long NAF section. (a) The image from the intermediate basin illustrates a sharp fault with a very narrow (<1 m) deformation zone. The southeast dipping scarp appears fresh. (b) Highly linear faults with minor scarps have been observed at the western end of the shelf. The scarps are partially buried with sediments deriving from the shelf area. (c) A scarp-in-scarp morphology has been documented in the shelf section of the NAF. The total height (at black arrows) is measured as $\sim 7 \pm 0.5$ m, therefore the lower scarp is necessarily less than 1 m high and possibly represents the latest faulting event in the region. (d) Shows the eastern tip of the pull-apart basin 1 shown in Fig. 3. The given scale applies to all SSS images. (e) and (f) Photographs of the surface ruptures of the 1999 Düzce earthquake formed along hill slopes show the geometry and location similarity between offshore and inland ruptures (photographs from Pucci *et al.* 2006 and Aydın & Kalafat 2002, respectively).

deformation of the last few surface rupturing events. The side-scan-sonar track covers also the pull-apart basin (2) illustrated in Fig. 3 (Fig. 12). The strong reflectivity on the north compared to the south indicates that the northern scarp is significantly higher, steeper, inclined to the south, and necessarily experiences more slip. A smaller inner pull-apart basin is visible on the southeastern margin of the basin. The basin-in-basin morphology marks the dilatation strike-slip dominant deformation.

Ustaömer *et al.* (2008) document several mass wasting morphologies, canyons and gullies in the Gulf of Saros. Our high-resolution multibeam bathymetry and the side-scan sonar data provide further details on these structures. Fig. 3 illustrates three canyons on the northern margin of the intermediate basin. These canyons have a width of 300–600 m; from east to west. The side-scan-sonar survey revealed additional channels of smaller size at a nearby location (see Figs 3 and 13). They occur at 20° to 40° slopes and their width ranges from 10 to 15 m. Further east we document similar channels and debris flows at slopes of 20°–30°. The channel widths are comparable in size. The associated debris flows are notable in the sonar image as dark reflections The debris can be traced for 20–30 m southward into the depocentre of the basin and demonstrate the environment of mass movement within the Gulf of Saros.

5 DISCUSSION

5.1 Young earthquake scarps

The above-given descriptions and analysis demonstrate new and presently the utmost details of the surficial structure and morphology of the NAF in the Gulf of Saros. The details shed light on the fault's structural complexity and reveal the existence of several young earthquake scarps. The scarps are well preserved and appear nearly continuous along the entire 37-km-long surveyed section. Their height differs from 1 to 10 m and incorporates the actual cumulative displacement of multiple surface faulting events. The well-preserved shape of the scarp crests suggests that erosional processes are at negligible levels for the current lifetime of these structures. Locally, and particularly eastwards some scarps are partially or completely buried with sediments that derive from the basin margin slopes and the Kavak river in the east. Hence some scarps may represent the minimum total offset. The scarps observed at the inner basin are on splays that strike 20° to 40° NW (Fig. 7). The two northern scarps are 10.2 and 4.3 m in height (Fig. 7). The

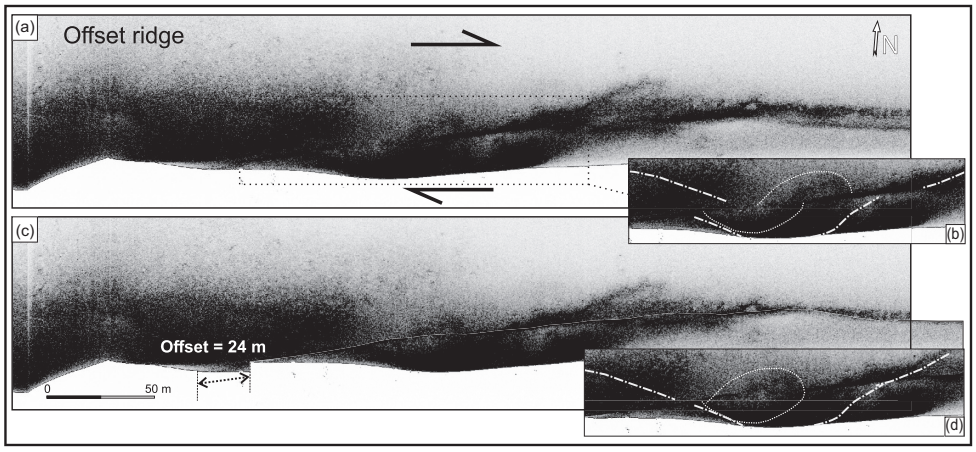

Figure 11. Side-scan sonar image from the shelf section (see Fig. 4 for location). The image corresponds to a rectilinear section of the NAF. A small ridge on the southern fault block appears to be displaced by 24 m. White dashed–dotted lines represent the foothill margin of the ridge (a, b). The white dotted line shows the base of a higher slope at the top of the hill. A reconstruction of the submarine morphology shows a fit with the escarpments. SAR_SS03.10H (c, d).

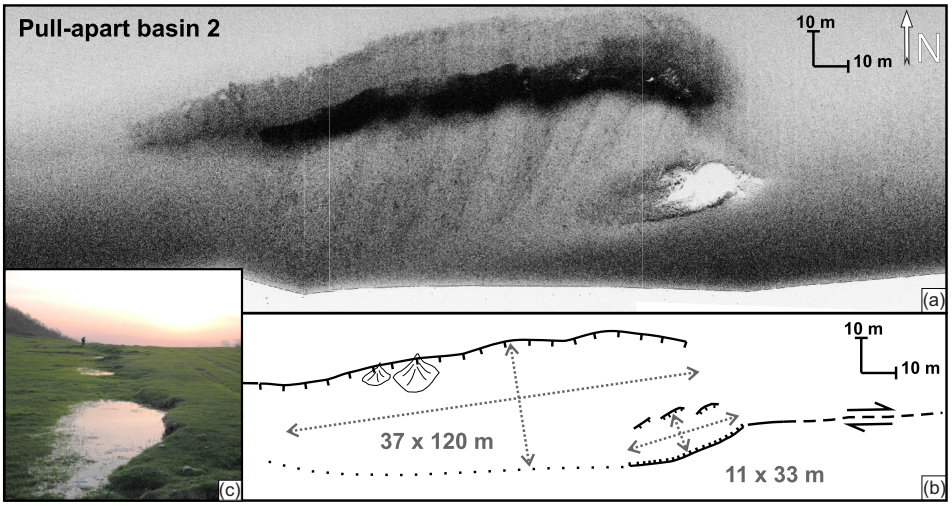

Figure 12. The side-scan sonar image exposes a basin-in-basin morphology in the shelf section (see Fig. 3 for location; profile SAR_SS03.014H). The scarp height near the fans is approximately 18 ± 1 m. The lower-right depression is significantly smaller and may be produced during a single surface faulting event. Such depressions (sagponds) have occurred during both the 17 August and 12 November 1999 Düzce earthquake (photo by S. Pucci, sagpond on the 12 November rupture)

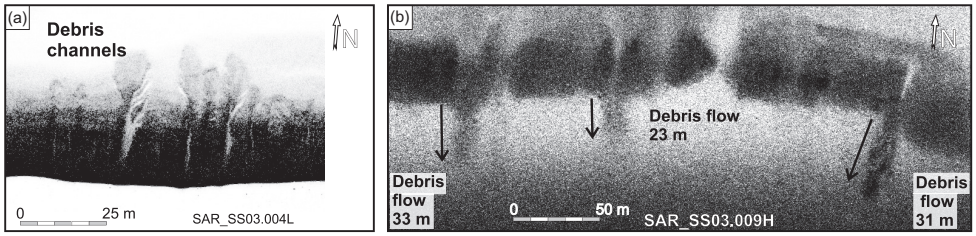

Figure 13. We have documented several submarine canyons of different scales along the fault. (a) A sonar image show canyons from the intermediate basin with channel widths ranging from 5 to 15 m. (b) A sonar image showing similar canyons and related debris flows reaching a distance of 23–33 m from the channel apex. The flow deposits appear as young structures since they are not eroded or buried, preserving their geometry. Therefore, these debris flows might have been triggered by the latest seismic events such as the 1912 earthquakes.

depth of the central depression is 1 m (Fig. 8). Scarps and sagponds with similar dimensions were formed during the 17 August 1999 Kocaeli earthquake rupture (M_w 7.4) on the eastern coast of the Sea of Marmara. Barka *et al.* (2002) and Klinger *et al.* (2003) report an 8-m-high scarp on the Gölcük-Kavaklı splay fault and document 2 m vertical and 1.1 m right-lateral coseismic slip (Fig. 7c). The scarp-in-scarp morphology, the orientation, and the amount of slip observed inland are comparable to our observations in the inner

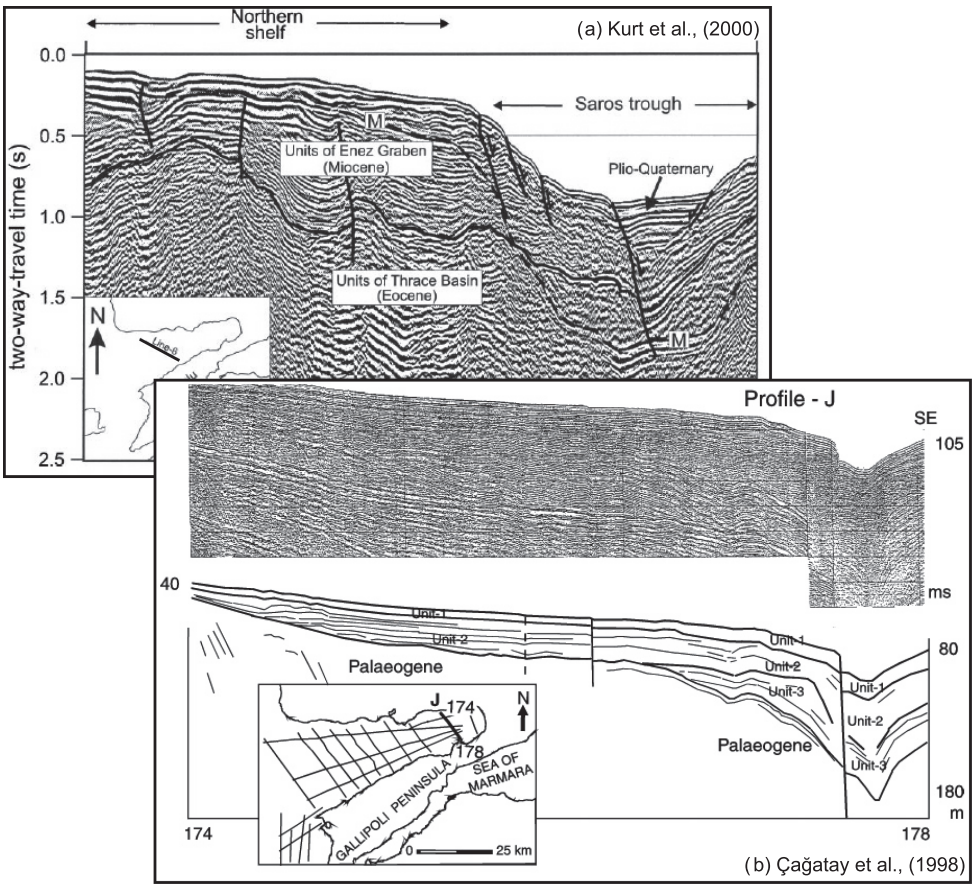

Figure 14. The structure of the NAF is accessible from earlier seismic reflection studies in the region. (a) Multichannel seismic section across the inner Saros basin showing the NAF as a south-dipping major fault. Smaller synthetic and antithetic faults contribute to the transtensional deformation (Kurt *et al.* 2000). (b) the sparker image from Çağatay *et al.* (1998) across the shelf area shows the NAF as a single through-going fault.

Saros basin. Therefore, we consider that the 1 m depression and 1–2-m-slip of the scarps can be attributed to the most recent 9 August 1912–M_w 7.4 and/or the 13 September 1912–M_s 6.8 earthquakes. Other fresh structures such as the depressions observed along the shelf (Fig. 12) contribute to our reasoning since they can be considered as equivalents of the several inland sagponds formed along the Ganos fault, the 17 August 1999 Kocaeli (M_w 7.4) and 12 November 1999 Düzce (M_w 7.2) ruptures.

5.2 Fault structure and major complexities

The presented data set does not only document the deformation of recent faulting events but also allows us to infer the complexity of the NAF which is an important factor controlling the faulting behavior during an earthquake. The high-resolution multibeam bathymetry depicts a straight main fault that is accompanied by minor fault bends, step-overs and short splays. The simplicity of the fault exists at several scales. The side-scan sonar images provide close-up views of 1- to 3-km-long segments that form dilatational and compressional step-overs of less than 150 m width (Figs 3, 10, 12). The multibeam bathymetry discloses geometrical characteristics at a larger scale. Westwards, the NAF forms a 6-km-long and 200-m-wide depression bounded with a strike-slip fault in the south and normal fault splays in the north; signifying a typical negative-flower structure morphology (Fig. 4a). The 3-km-wide intermediate basin at its west resembles this morphology at a larger scale where the strike-slip deformation occurs on the north and normal faulting in the south (Fig. 5). A similar structural setting recurs within the inner basin at the largest scale (Figs 2 and 6). At the entrance of the inner basin, the NAF bifurcates. The northern branch makes a 10° releasing bend and continues as a slightly sinusoidal strike-slip fault. At the western limit of the Gulf of Saros, the fault forms a 20° releasing bend. The south of the basin consists of a set of en-echelon-orientated normal faults (Fig. 2).

The transtensional tectonic morphology is an expression of the NAF structure towards depth. Earlier seismic reflection profiles cross-cutting the shelf and the inner basin illustrate the NAF as a single through-going fault that is accompanied by secondary splay faults displacing Quaternary deposits (Fig. 14, Çağatay *et al.* 1998; Kurt *et al.* 2000). Nevertheless, from the eastern limit of the inner basin to the Kavak shoreline, the entire 35-km-long section displays a straight, simple main strike-slip fault with minor complexities that are unlikely to function as a rupture barrier (Wesnousky 2006).

5.3 Mass wasting events: debris flows and seismo-turbidites

The canyon and gullies observed in the intermediate shallow basin and along the fault in the shelf depict debris flows. The size of the flows and the freshness of the structures suggests that these deposits are the result of a recent single event, likely by an earthquake. The most recent earthquakes that are sufficiently close to trigger such debris flows are the 1912 (M_s 7.4 and M_s 6.8), the 1975 (M_s 6.6) and the 2003 (M_w 5.7) earthquakes.

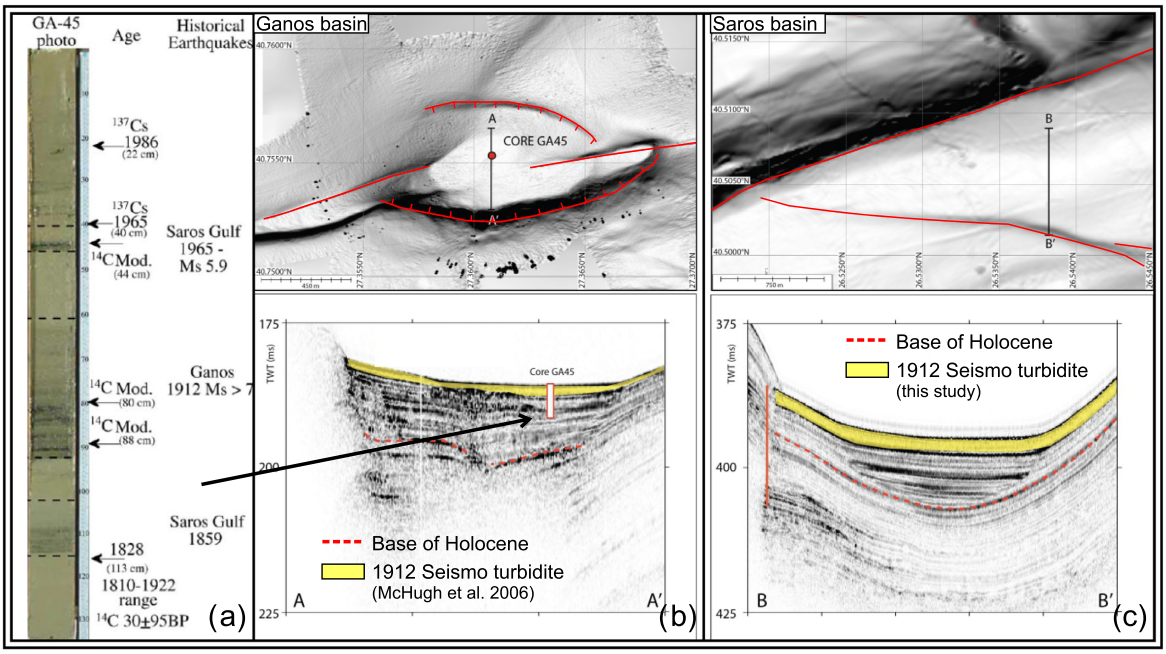

Figure 15. (a) In the core G-45 from the Ganos basin (Fig. 5), the coarse basal layers of seismoturbidites are visible as dark layers (modified from McHugh *et al.* 2006). The 1965 (M_s 5.9) earthquake lies in the North Aegean Trough and is approximately 100 km west of the Saros basin and 223 km away from the Ganos basin. Considering the distance and size of the 1965 event and uncertainties associated with the radiometric dating of resedimented deposits, the 1975 (M_s 6.6) is more likely to be the trigger for this seismo-turbidite. A comparison of the multibeam and seismic reflection profiles from the Ganos basin (b) and the intermediate Saros shallow basin (c) suggests that the uppermost units (yellow) might represent the homogenite-seismo-turbidites.

Besides, mass-flows (seismoturbidites) have been documented for the 9 August 1912 earthquake in the Ganos basin of the Sea of Marmara (Figs 2 and 15, McHugh *et al.* 2006). The Ganos Basin depocentre is filled by sand-rich layers with a sharp basal erosional contact overlain by fining upwards silty units that grade into a thick homogenous mud. The geophysical, geochemical, and sedimentological characters of these sediment beds (transparent seismic facies, TOC rich layers, sandy base overlain by fining upwards sediments) suggest they are seismically triggered resedimented deposits (Fig. 15a, McHugh *et al.* 2006). Their structure and geochemical features are very similar to seismo-turbidites described in other basins of the Sea of Marmara (Çağatay *et al.* 2012; Yakupoğlu *et al.* 2019) and Mediterranean Sea (Polonia *et al.* 2017).

The most recent seismo-turbidites in the Ganos basin were correlated to regional historic earthquakes in the region, based on their emplacement time as deduced through radiometric dating (Fig. 15, McHugh *et al.* 2006). The 1912 Mürefte-Şarköy seismo-turbidite, which was sampled during the Urania 2001 cruise, can be traced in the chirp profiles throughout the basin floor as a 3-m-thick deposit (Figs 15b,c). The core site was selected where the turbidite thickness was minimum so both the top and base of the seismo-turbidite could be recovered (Fig. 15).

CHIRP seismic profile M11_018 (Fig. 15c) was collected in the intermediate shallow basin and shows a tectonically controlled basin depocentre developing between the main NAF to the north and the antithetic normal fault associated with the seafloor scarp on the multibeam map (Figs 5 and 15). The dotted red line represents the base of Holocene sediments, which is about 4–5 m thick on the basin slopes (Fig. 8, orange line), in agreement with sedimentation rates in the Sea of Marmara deep basins reported as 43 to 100 cm kyr^{-1} (Çağatay & Uçarkuş 2019; Makaroğlu *et al.* 2020, and references therein). The Holocene section thickens in the shallow basin depocentre which is driven by gravitational processes and tectonic subsidence. In this basin, the thickness of Holocene sediments is three times larger than the basin margins and implies tectonic subsidence during the Holocene. The shallow basin depocentre is filled by a ≈10-m-thick sediment packet characterized by an alternation of transparent thin layers and high amplitude reflectors. The uppermost transparent layer (about 2 m thick) is very similar to the Ganos homogenite-mud bed and the very high amplitude basal reflector to the sandy basal turbidite unit. These characters suggest that its deposition might be seismically triggered and related to the most recent 1912 or 1975 earthquakes.

5.4 The western termination of the 1912 rupture(s)

The foregoing discussion describes young earthquake scarps likely to be produced by a single recent event and shows that the eastern 35-km-long section of the NAF in the gulf consists of 1- to 7-km-long linear segments that form dilatational and compressional step-overs of less than 200 m width. These complexities are minor discontinuities unlikely to arrest a rupture propagation (Wesnousky 2006). Therefore, taking into account the 4.5 m coseismic channel displacement at the Kavak shore (Rockwell *et al.* 2009) and the 100–160 km rupture length calculated for the 9 August 1912 earthquake (Altunel *et al.* 2004; Armijo *et al.* 2005; Karabulut *et al.* 2006; Aksoy *et al.* 2010; Aksoy 2021) we consider that the 9 August shock ruptured westwards the entire 35 km straight section and continued until the bifurcation and the 10° dilatational bend in the inner basin (Figs 2 and 6). The 9 August 1912 earthquake (M_w 7.4) was followed by a large shock on 13 September 1912 (M_s 6.8), which ruptured the westward continuation of the 9 August

shock (Aksoy *et al.* 2010). Therefore, the scarps illustrated in Figs 7 and 8 may represent the rupture of the 13 September shock. The sections ruptured by the two events may slightly differ along strike or overlap partially. Nevertheless, the distribution of instrumental seismicity supports the suggested locations for the two ruptures. Since 1912, a few $M > 6$ earthquakes have occurred along the western tip of NAF (Fig. 1). The most recent, 24 May 2014 M_w 6.9 earthquake occurred offshore, approximately 20 km SW of the Gökçeada island, and ruptured a 90-km-long section of the NAF (max coseismic slip 2.5 m; Konca *et al.* 2018). The eastern aftershocks overlap with the seismicity of the 1975 M_s 6.6 and 2003 M_w 5.7 earthquakes (Karabulut *et al.* 2006). The tip of the 2014 aftershock activity reaches the bifurcation of the NAF (Fig. 1) and signifies an approximate limit for the ruptured segment (Konca *et al.* 2018). The section east of the bifurcation is aseismic and indicative of a locked fault (Karabulut *et al.* 2006; Ergintav *et al.* 2014; Konca *et al.* 2018). This distribution of seismicity suggests that the bifurcation may have functioned as a barrier and therefore corresponds to an endpoint of the earthquake segment that has ruptured during the 1912 earthquake(s).

If the 1912 earthquakes ruptured a 150–160 km section of the NAF (Karabulut *et al.* 2006; Aksoy 2021) with a western limit at the entrance of the inner Saros basin, then the eastern limit of the 9 August 1912 rupture is necessarily somewhere within the Central basin as suggested by Armijo *et al.* (2005) and Aksoy *et al.* (2010). This leaves about 100-km-long seismic gap between the 1999 and 1912 ruptures.

6 CONCLUSION

Our high-resolution geophysical data allowed mapping the subaqueous fine-scale morphology and structure of the NAF in the Gulf of Saros. We determined fresh earthquake scarps, pull-apart basins, pressure ridges, offset structures, and debris flows (seismoturbidites) along the 37-km-long fault section. Particularly the scarps that are <1 m in height appear as single event morphology. We lack of any dating results for these morpho-tectonic structures, however the well-defined inland extend of the 1912 rupture (45 km) and the 100–160 km total rupture length defined from multiple parameters by previous studies (Altunel *et al.* 2004; Armijo *et al.* 2005; Karabulut *et al.* 2006; Aksoy *et al.* 2010) implies the rupture has extended significantly towards the Gulf of Saros. Therefore, we attribute some of these structures to the 9 August and 13 September 1912 earthquakes. We are not able to distinguish the rupture of the 9 August from that of the 13 September aftershock, however, the distribution of fresh scarps, the 3-D structural simplicity of the mapped fault section, lack of any major complexity along strike, and the recent seismicity suggest that the 1912 rupture(s) reached 37 km offshore to the eastern entrance of the inner Saros basin and likely terminated at the bifurcation within the inner Saros basin. Considering the total rupture length of the 1912 events, this outcome has implications for the eastern extension of the 9 August 1912 rupture in the Sea of Marmara and therefore contributes to the seismic hazard evaluation for the entire urban area around the Sea of Marmara coast including the metropolis Istanbul.

ACKNOWLEDGEMENTS

We thank Captain Lubrano, Captain Lembo, Captain Gentile and the crew of R/V Urania for their invaluable assistance during all the Sea of Marmara and NE Aegean cruises. Naci Görür coordinated the bilateral Turkish–Italian scientific project in Marmara. The İstanbul Metropolitan Municipality (IBB) funded partially the İTÜ EMCOL (Turkey) & CNR ISMAR (Italy) project 'Evaluating the Seismic Risk in the Sea of Marmara' (Turkish title: Marmara Denizi'nde Deprem Riskinin Değerlendirilmesi) during the 2005 Urania cruise. The side-scan-sonar and chirp profile data used in the paper are available at the ISMAR repository at http://www.ismar.cnr.it/products/data-sharing.

Author Contribution Statement: All authors participated in the data collection stage. LG, MEA, ŞÖ and AZY did the data processing. MEA, LG, AP, MM and MNÇ did the data analysis and wrote the manuscript. The final version of the manuscript has been revised by all authors.

DATA AVAILABILITY

The side-scan-sonar and chirp profile data used in the article are available at the ISMAR repository at http://www.ismar.cnr.it/products/data-sharing. Readers may also contact the authors to request the data used in the paper.

REFERENCES

Aksoy, M.E., 2021. The 9 August 1912 Mürefte-Şarköy earthquake of the North Anatolian fault, *Mediterran. Geosci. Rev.,* **3,** 95–114.

Aksoy, M.E., Meghraoui, M., Vallee, M. & Çakır, Z., 2010. Rupture characteristics of the A.D. 1912 Mürefte (Ganos) earthquake segment of the North Anatolian fault (western Turkey), *Geology,* **38,** 991–994.

Akyüz, H.S., Hartleb, R., Barka, A., Altunel, E., Sunal, G., Meyer, B. & Armijo, R.. 2002. Surface Rupture and Slip Distribution of the 12 November 1999 Duzce Earthquake (M 7.1), North Anatolian Fault, Bolu, Turkey, *Bull. Seismol. Soc. Am.,* **92**(1) 61–66.

Altınok, Y., Alpar, B. & Yaltırak, C., 2003. Şarköy - Mürefte 1912 Earthquake's Tsunami, extension of the associated faulting in the Marmara Sea, Turkey, *J. Seismol.,* **7**(3), 329–346.

Altunel, E., Meghraoui, M., Akyüz, H.S. & Dikbaş, A., 2004. Characteristics of the 1912 co-seismic rupture along the North Anatolian Fault Zone (Turkey): implications for the expected Marmara earthquake, *Terra Nova,* **16,** 198–204.

Ambraseys, N.N. & Jackson, J.A. 2000. Seismicity of the Sea of Marmara (Turkey) since 1500, *Geophys. J. Int.,* **141**(), F1–F6.

Ambraseys, N.N., 1970. Some characteristic features of the Anatolian fault zone, *Tectonophysics,* **9,** 143–165.

Ambraseys, N.N. & Finkel, C.F., 1987. The Saros-Marmara earthquake of 9 August 1912, *Earthq. Eng. Struct. Dynam.,* **15,** 189–211.

Ambraseys, N.N. & Zatopek, A., 1969. The Mudurnu Valley, West Anatolia, Turkey, earthquake of 22 July 1967, *Bull. seism. Soc. Am.,* **59,** 521–589.

Armijo, R. *et al.*, 2005. Submarine fault scarps in the Sea of Marmara pull-apart (North Anatolian Fault): implications for seismic hazard in Istanbul, *Geochem. Geophys. Geosyst.,* **6,** Q06009,

Armijo, R., Meyer, B., Hubert, A. & Barka, A., 1999. Westward propagation of the North Anatolian fault into the northern Aegean: timing and kinematics, *Geology,* **27,** 267–270.

Aydın, A. & Kalafat, D., 2002. Surface ruptures of the 17 August and 12 November 1999 İzmit and Düzce earthquakes in Northwestern Anatolia, Turkey: their tectonic and kinematic significance and the associated damage, *Bull. seism. Soc. Am.,* **92,** 95–106.

Barka, A. *et al.*, 2002. The surface rupture and slip distribution of the 17 August 1999 Izmit earthquake (M 7.4), North Anatolian Fault, *Bull. seism. Soc. Am.,* **92,** 43–60.

Barka, A., 1996. Slip distribution along the North Anatolian fault associated with the large earthquakes of the period 1939 to 1967, *Bull. seism. Soc. Am.,* **86,** 1238–1254.

Barka, A. & Kadinsky-Cade, K., 1988. Strike-slip fault geometry in Turkey and its influence on earthquake activity, *Tectonics,* **7,** 663–684.

Bohnhoff, M., Bulut, F., Dresen, G., Malin, P.E., Eken, T. & Aktar, M., 2013. An earthquake gap south of Istanbul, *Nat. Commun.,* **4,** 1999.

Çağatay, M.N. *et al.*, 1998. Geological evolution of the Gulf of Saros, NE Aegean Sea, *Geo-Mar. Lett.,* **18,** 1–9.

Çağatay, M.N. *et al.*, 2012. Sedimentary earthquake records in the İzmit Gulf, Sea of Marmara, Turkey, *Sediment. Geol.,* **282,** 347–359.

Çağatay, M.N. & Uçarkuş, G., 2019. Morphotectonics of the Sea of Marmara: basins and highs on the North Anatolian continental transform plate boundary, in *Transform Plate Boundaries and Fracture Zones,* ed. Duarte, J., Elsevier, doi:10.1016/B978-0-12-812064-4.00016-5.

Çakır, Z., Chabalier, J.-B.d., Armijo, R., Meyer, B., Barka, A. & Peltzer, G.. 2003. Coseismic and early post-seismic slip associated with the 1999 Izmit earthquake (Turkey), from SAR interferometry and tectonic field observations, *Geophys. J. Int.,* **153**(1)93–110.

Chorowicz, J., Dhont, D. & Gündoğdu, N., 1999. Neotectonics in the eastern North Anatolian fault region (Turkey) advocates crustal extension: mapping from SAR ERS imagery and digital elevation model, *J. Struct. Geol.,* **21,** 511–532.

Drab, L., Hubert Ferrari, A., Schmidt, S. & Martinez, P., 2012. The earthquake sedimentary record in the western part of the Sea of Marmara, Turkey, *Nat. Hazards Earth Syst. Sci.,* **12,** 1235–1254.

Emre, Ö., Kondo, H., Özalp, S. & Elmacı, H., 2020. Fault geometry, segmentation and slip distribution associated with the 1939 Erzincan earthquake rupture along the North Anatolian fault, Turkey, *Geol. Soc., Lond., Spec. Publ.,* **501,** SP501–2019–2141.

EMSC. 2020. Earthquake Catalogue of European-Mediterranean Seismological Centre. Retrieved from https://www.emsc-csem.org/Earthquake/?filter=yes, Retrieved 2020.10.10.

Ergintav, S. *et al.*, 2014. Istanbul's earthquake hot spots: geodetic constraints on strain accumulation along faults in the Marmara seismic gap, *Geophys. Res. Lett.,* **41,** 5783–5788.

Gasperini, L., Polonia, A., Bortoluzzi, G., Henry, P., Pichon, X.L., Tryon, M., Çağatay, N. & Géli, L., 2011a. How far did the surface rupture of the 1999 İzmit earthquake reach in Sea of Marmara?, *Tectonics,* **30**(1),.

Gasperini, L., Polonia, A. & Çağatay, M.N., 2018. Fluid flow, deformation rates and the submarine record of major earthquakes in the Sea of Marmara, along the North-Anatolian Fault system, *Deep Sea Res. Part II,* **153,** 4–16.

Gasperini, L., Polonia, A., Çağatay, M.N., Bortoluzzi, G. & Ferrante, V., 2011b. Geological slip rates along the North Anatolian Fault in the Marmara region, *Tectonics,* **30,** 1–14.

Gasperini, L. & Stanghellini, G., 2009. SeisPrho: an interactive computer program for processing and interpretation of high-resolution seismic reflection profiles, *Comput. Geosci.,* **35,** 1497–1507.

Gasperini, L., Stucchi, M., Cedro, V., Meghraoui, M., Uçarkuş, G. & Polonia, A., 2021. Active fault segments along the North Anatolian Fault system in the Sea of Marmara: implication for seismic hazard, *Mediterran. Geosci. Rev.,* **3,** 29–44.

Géli , L., Henry, P. & Çağatay, M.N. 2021. A review of 20 years (1999–2019) of Turkish–French collaboration in marine geoscience research in the Sea of Marmara, *Mediterranean Geoscience Reviews,* **3**(1)3–27.

Hubert-Ferrari, A., Barka, A., Jacques, E., Nalbant, S.S., Meyer, B., Armijo, R., Tapponnier, P. & King, G.C.P., 2000. Seismic hazard in the Marmara Sea region following the 17 August 1999 Izmit earthquake, *Nature,* **404,** 269–273.

Karabulut, H., Roumelioti, Z., Benetatos, C., Ahu Kömec, M., Özalaybey, S., Aktar, M. & Kiratzi, A., 2006. A source study of the 6 July 2003 (Mw 5.7) earthquake sequence in the Gulf of Saros (Northern Aegean Sea): seismological evidence for the western continuation of the Ganos fault, *Tectonophysics,* **412,** 195–216.

Klinger, Y. *et al.*, 2003. Paleoseismic evidence of characteristic slip on the western segment of the North Anatolian Fault, Turkey, *Bull. seism. Soc. Am.,* **93,** 2317–2332.

KOERI, 2020. Earthquake Catalogue of Regional Earthquake-Tsunami Monitoring Center. Retrieved from, http://www.koeri.boun.edu.tr/sismo/2/earthquake-catalog/. Available from Boğaziçi University - Kandilli Observatory and Earthquake Research Institute Earthquake Catalog Search System Retrieved 2020.03.01.

Konca, A.Ö., Çetin, S., Karabulut, H., Reilinger, R., Doğan, U., Ergintav, S., Çakır, Z. & Tarı, E., 2018. The 2014, Mw6.9 North Aegean earthquake: seismic and geodetic evidence for coseismic slip on persistent asperities, *Geophys. J. Int.,* **213,** 1113–1120.

Kondo, H. *et al.*, 2005. Slip distribution, fault geometry, and fault segmentation of the 1944 Bolu-Gerede earthquake rupture, North Anatolian Fault, Turkey, *Bull. seism. Soc. Am.,* **95,** 1234–1249.

Kurt, H., Demirbağ, E. & Kuşcu, I., 2000. Active submarine tectonism and formation of the Gulf of Saros, Northeast Aegean Sea, inferred from multi-channel seismic reflection data, *Mar. Geol.,* **165,** 13–26.

Lange, D., *et al.*, 2019. Interseismic strain build-up on the submarine North Anatolian Fault offshore Istanbul, *Nature Communications,* **10**(1)3006.

Langridge, R.M., Stenner, H.D., Fumal, T.E., Christofferson, S.A., Rockwell, T.K., Hartleb, R.D., Bachhuber, J. & Barka, A.A., 2002. Geometry, slip distribution, and kinematics of surface rupture on the Sakarya Fault Segment during the 17 August 1999 Izmit, Turkey, Earthquake, *Bull. seism. Soc. Am.,* **92,** 107–125.

Le Pichon, X. *et al.*, 2001. The active Main Marmara Fault, *Earth planet. Sci. Lett.,* **192,** 595–616.

Le Pichon, X., Chamot-Rooke, C., Rangin, N. & Şengör, A.M.C. 2003. The North Anatolian fault in the Sea of Marmara, *J. Geophys. Res.,* **108**(B4) 2179.

Makaroğlu, Ö., Nowaczyk, N.R., Eriş, K.K. & Çağatay, M.N., 2020. High-resolution palaeomagnetic record from Sea of Marmara sediments for the last 70 ka, *Geophys. J. Int.,* **222,** 2024–2039.

McHugh, C.M.G., Seeber, L., Cormier, M.-H., Dutton, J., Çağatay, M.N., Polonia, A., Ryan, W.B.F. & Görür, N., 2006. Submarine earthquake geology along the North Anatolia Fault in the Marmara Sea, Turkey: a model for transform basin sedimentation, *Earth planet. Sci. Lett.,* **248,** 661–684.

McKenzie, D., 1972. Active tectonics of the Mediterranean region, *Geophys. J. R. astr. Soc.,* **30,** 109–185.

McNeill, L.C., Mille, A., Minshull, T.A., Bull, J.M., Kenyon, N.H. & Ivanov, M., 2004. Extension of the North Anatolian Fault into the North Aegean Trough: evidence for transtension, strain partitioning, and analogues for Sea of Marmara basin models, *Tectonics,* **23,** 12.

Meghraoui, M., Aksoy, M.E., Akyüz, H.S., Ferry, M., Dikbaş, A. & Altunel, E., 2012. Paleoseismology of the North Anatolian Fault at Güzelköy (Ganos segment, Turkey): size and recurrence time of earthquake ruptures west of the Sea of Marmara, *Geochem. Geophys. Geosyst.,* **13**(4), doi:10.1029/2011GC003960.

Meghraoui, M., Toussaint, R. & Aksoy, M.E., 2021. The slip deficit on the North Anatolian Fault (Turkey) in the Marmara Sea: insights from paleoseismicity, seismicity and geodetic data, *Mediterran. Geosci. Rev.,* **3,** 45–56.

Mihailovic, J., 1927. Trusne katastrofe na Mramornome moru sa narocitim pogledom na opstu seizmicnost Mramornoga mora i njegovih obala, Srpska kraljevska akademija, posebna izdanja, knj. LXV - Prirodnjacki i matematicki spisi, knj. 16, 303 str., 78 sl., 46 skica, 6 dijagrama, 1 karta,, **Vol. 65**. Belgrade. pp. 1–303.

Okay, A.I., Tüysüz, O. & Kaya, S., 2004. From transpression to transtension: changes in morphology and structure around a bend on the North Anatolian Fault in the Marmara region, *Tectonophysics,* **391,** 259–282.

Pamir, H.N. & Ketin, I., 1941. Das anatolische Erdbeben Ende 1939, *Geol. Rundsch.,* **32,** 279–287.

Parsons, T., Toda, S., Stein, R.S., Barka, A. & Dieterich, J.H., 2000. Heightened Odds of Large Earthquakes Near Istanbul: an Interaction-Based Probability Calculation, *Science,* **288,** 661–665.

Philippon, M., Brun, J.-P., Gueydan, F. & Sokoutis, D., 2014. The interaction between Aegean back-arc extension and Anatolia escape since Middle Miocene, *Tectonophysics,* **631,** 176–188.

Polonia, A. *et al.*, 2002. Exploring submarine earthquake geology in the Marmara Sea, *EOS, Trans. Am. geophys. Un.,* 83.

Polonia, A. *et al.*, 2004. Holocene slip rate of the North Anatolian Fault beneath the Sea of Marmara, *Earth planet. Sci. Lett.,* **227,** 411–426.

Polonia, A., Nelson, C.H, Romano, S., Vaiani, S.C., Colizza, E., Gasparotto, G. & Gasperini, L. 2017. A depositional model for seismo-turbidites

in confined basins based on Ionian Sea deposits, *Mar. Geol.,* **384,** 177–198.

Pucci, S., Palyvos, N., Zabcı, C., Pantosti, D. & Barchi, M. 2006. *J. geophys. Res.,* **111**(B6), doi:10.1029/2004JB003578.

Reilinger, R.E. *et al.*, 2006. GPS constraints on continental deformation in the Africa-Arabia-Eurasia continental collision zone and implications for the dynamics of plate interactions, *J. geophys. Res.,* **111**(B5), doi:10.1029/2005JB004051.

Ribot, M., Klinger, Y., Jónsson, S., Avsar, U., Pons-Branchu, E., Matrau, R. & Mallon, F.L. 2021 Active Faults' Geometry in the Gulf of Aqaba, Southern Dead Sea Fault, Illuminated by Multibeam Bathymetric Data , *Tectonics,* **40**(4) 1–13.

Rockwell, T.K. *et al.*, 2009. Palaeoseismology of the North Anatolian Fault near the Marmara Sea: implications for fault segmentation and seismic hazard, *Geol. Soc., Lond., Spec. Publ.,* **316,** 31–54.

Rockwell, T.K., Barka, A., Dawson, T., Akyüz, S. & Thorup, K., 2001. Paleoseismology of the Gaziköy-Saros segment of the North Anatolia fault, northwestern Turkey: comparison of the historical and paleoseismic records, implications of regional seismic hazard, and models of earthquake recurrence, *J. Seismol.,* **5,** 433–448.

Rockwell, T.K., Lindvall, S., Dawson, T., Langridge, R., Lettis, W. & Klinger, Y., 2002. Lateral offsets on surveyed cultural features resulting from the 1999 Izmit and Düzce Earthquakes, Turkey, *Bull. seism. Soc. Am.,* **92,** 79–94.

Schmittbuhl, J., Karabulut, H., Lengliné, O. & Bouchon, M., 2015. Seismicity distribution and locking depth along the Main Marmara Fault, Turkey, *Geochem. Geophys. Geosyst.,* **17,** 954–965.

Şengör, A.M.C., Tüysüz, O., İmren, C., Sakınç, M., Eyidoğan, H., Naci, G., Le Pichon, X. & Rangin, C., 2005. The North Anatolian Fault : a New Look, *Annu. Rev. Earth planet. Sci.,* **33,** 37–112.

Taymaz, T., Jackson, J.& & McKenzie, D., 1991. Active tectonics of the north and central Aegean Sea, *Geophys. J. Int.,* **106**(2) 433–490.

Tüysüz, O., Barka, A. & Yiğitbaş, E.. 1998. Geology of the Saros graben and its implications for the evolution of the North Anatolian fault in the Ganos-Saros region, northwestern Turkey, *Tectonophysics,* **293,** 105–126.

Uçarkuş, G., Çakır, Z. & Armijo, R., 2011. Western Termination of the Mw 7.4, 1999 İzmit Earthquake Rupture: implications for the Expected Large Earthquake in the Sea of Marmara, *Turkish J. Earth Sci,* **20,** 379–394.

Ustaömer, T. *et al.*, 2008. Faulting, mass-wasting and deposition in an active dextral shear zone, the Gulf of Saros and the NE Aegean Sea, NW Turkey, *Geo-Mar. Lett.,* **28,** 171–193.

Wesnousky, S.G., 2006. Predicting the endpoints of earthquake ruptures, *Nature,* **444,** 358–360.

Yakupoğlu, N., Uçarkuş, G., Kadir Eriş, K., Henry, P. & Çağatay, M.N., 2019. Sedimentological and geochemical evidence for seismoturbidite generation in the Kumburgaz Basin, Sea of Marmara: implications for earthquake recurrence along the Central High Segment of the North Anatolian Fault, *Sediment. Geol.,* **380,** 31–44.